# Characterization of plasma catalytic decomposition of methane: role of atomic O and reaction mechanism

**Yudong Li,[1] Jingkai Jiang,[2] Michael Hinshelwood,[1] Shiqiang Zhang,[1] Peter J. Bruggeman,[2] and Gottlieb S. Oehrlein[1]***

[1] Department of Materials Science and Engineering and the Institute for Research in Electronics and Applied Physics, University of Maryland, College Park, MD 20742, USA

[2] Department of Mechanical Engineering, University of Minnesota, Minneapolis, MN 55455, USA

*Corresponding author: oehrlein@umd.edu

## Abstract

In this work, we investigated atmospheric pressure plasma jet (APPJ)-assisted methane oxidation over a Ni-$SiO_2$/$Al_2O_3$ catalyst. We evaluated possible reaction mechanisms by analyzing the correlation of gas phase, surface and plasma-produced species. Plasma feed gas compositions, plasma powers, and catalyst temperatures were varied to expand the experimental parameters. Real-time Fourier-transform infrared spectroscopy (FTIR) was applied to quantify gas phase species from the reactions. The reactive incident fluxes generated by plasma were measured by molecular beam mass spectroscopy (MBMS) using an identical APPJ operating at the same conditions. A strong correlation of the quantified fluxes of plasma-produced atomic oxygen with that of $CH_4$ consumption, and CO and $CO_2$ formation implies that O atoms play an essential role in $CH_4$ oxidation for the investigated conditions. With the integration of APPJ, the apparent activation energy was lowered and a synergistic effect of 30% was observed. We also performed in-situ diffuse reflectance infrared Fourier-transform spectroscopy (DRIFTS) to analyze the catalyst surface. The surface analysis showed that surface CO abundance mirrored the surface coverage of $CH_n$ at 25 $^oC$. This suggests that $CH_n$ adsorbed on the catalyst surface as an intermediate species that was subsequently transformed into surface CO. We observed very little surface $CH_n$ absorbance at 500 $^oC$, while a ten-fold increase of surface CO and stronger $CO_2$ absorption were seen. This indicates that for a nickel catalyst at 500 $^oC$, the dissociation of $CH_4$ to $CH_n$ may be the rate-determining step in the plasma-assisted $CH_4$ oxidation for our conditions. We also found the CO vibrational frequency changes from 2143 $cm^{-1}$ for gas phase CO to 2196 $cm^{-1}$ for CO on a 25 $^oC$ catalyst surface, whereas the frequency of CO on a 500 $^oC$ catalyst was

2188 $cm^{-1}$. The change in CO vibrational frequency may be related to the oxidation of the catalyst.

## 1. Introduction

Plasma catalysis is a promising technique that may improve the efficiency of chemical processing using catalyst materials [1-3], and lower the temperature required to activate the catalyst [4, 5]. Plasma catalysis has been investigated for volatile organic compound (VOC) removal [6, 7], hydrocarbon reforming [8-11], ammonia production [12, 13] and others. Plasmas have also been used to synthesize catalysts [14, 15]. A synergistic effect, i.e., a higher conversion rate and lower activation energy for a combined approach relative to separate plasma or thermal catalysis driven conversions, have been reported in several publications [9, 16]. However, the mechanistic origins of the plasma-catalyst synergistic effect remain elusive.

Cold atmospheric pressure plasmas (CAPP) used in plasma catalysis are able to generate high energy electrons [17], ions, and highly reactive species including radicals and electronically excited species without large increase in gas temperatures [18-20]. This large variety of reactive species including the production of photons and electrical fields has not allowed to experimentally identify key species produced from the plasma that are responsible for plasma catalytic reactions [19]. The absence of such a correlation impedes the further development of the plasma-catalysis technique.

The methane oxidation to syngas reaction has many potential benefits compared to other methane reforming techniques [21]. Primarily, it is an exothermic reaction with a lower energy cost than other pathways [22]. Despite intense research efforts, the reaction pathways even without the presence of plasma remain subject to continued research. Two reaction pathways are mainly discussed: (i) Reforming mechanism: the $CH_4$ is first completely oxidized to $CO_2$ over the catalyst. Subsequently, $CO_2$ reforming of $CH_4$ takes place to produce CO, which is the secondary product [22-24]. (ii) Direct partial oxidation mechanism: $CH_4$ is dehydrated to $CH_n$

species on the catalyst which are then oxidized to CO, and CO is the primary product [25-28]. It should be noted that the temperature range and the state of the catalyst, e.g., reduced or unreduced, can have a significant influence on reaction pathways. The lack of a complete understanding of the pathways of thermal oxidation of $CH_4$ sets an obstacle for interpreting the mechanism of plasma-assisted $CH_4$ oxidation.

One of the difficulties in investigating the mechanism of plasma catalysis is the implementation of in-situ/operando surface characterization [29]. The rapid changes that occur on the catalyst surface can provide valuable information regarding the reaction pathways. However, the appearance of those surface species may be subtle and transient, making it difficult to capture such information, especially in the plasma-catalysis system where the plasma is generated in close contact with the catalyst providing challenges to perform in-situ surface characterization techniques. The high pressure environment also precludes the use of many surface characterization techniques standardly used in low pressure plasmas which require a vacuum environment [29]. Stere et al. described a novel design of a DBD plasma-catalysis system that allows in-situ surface characterization by DRIFTS to investigate plasma-assisted VOCs removal over three metal oxide catalysts [30].

In the past few years, we have developed a well-described non-thermal atmospheric pressure plasma jet [17, 20, 31, 32]-catalyst system that is capable of performing real-time downstream gas phase and operando surface analysis [11, 16, 29]. The key feature of such a design is the possibility to do in-situ surface characterization by DRIFTS. Since the plasma generation occurs remotely in the plasma jet and reactive species are convectively transported to the catalyst, easy access to the catalyst surface for external characterization is available. This approach has also key advantages for the measurement of the plasma-produced short-lived reactive species. The

APPJ-catalyst interaction in the decomposition of methane in this system has been extensively evaluated. Knoll et al. [16] investigated the behaviors of $CH_4$ and products of the reaction using different plasma parameters and catalyst temperatures. They found that the CO production was due primarily to the APPJ effect. The CO production was suppressed at high temperature while $CO_2$ production was enhanced. Spectral features obtained by DRIFTS were discussed and CO and $CO_2$ gases were found to be related with surface species. Zhang et al. [11] investigated the time-resolved response of surface CO and $CH_n$ species to catalyst temperature, plasma feed gas composition, and plasma-surface distance. They found that the surface CO formation was correlated with the removal of surface $CH_n$ by the APPJ when operating with high oxygen concentration in the feed gas.

Although much progress and understanding of the plasma-catalyst interaction have been accomplished, a comprehensive analysis of the connection between the plasma source and the plasma-catalytic reaction is still lacking. In this work, we characterized the downstream gas phase and the surface under various conditions using an IR spectrometer at the University of Maryland and quantified the plasma-produced reactive species flux using MBMS on an identical plasma jet operating at the same conditions at the University of Minnesota. A correlation between the measured gas phase species, reactive species produced by the APPJ, and surface species has been established, and the synergy effect has been evaluated. By combining all the measurements and performing correlations, we can draw conclusions about the key species contributing to the oxidation of $CH_4$ and shed light on the mechanism of the underpinning plasma-catalyst interaction.

## 2. Experimental setup and procedure

The plasma source used in this study was a RF driven APPJ running at 14.3 MHz frequency modulated by 20 kHz on/off duty cycle (20% on time and 80% off time). A high voltage tungsten pin was placed in the center of a dielectric quartz tube, whereas the grounded ring electrode was attached around the tube [16]. The properties of this APPJ have been extensively reported [17, 33, 34]. The APPJ was fed with 200 sccm Ar and 1, 2 or 3 sccm $O_2$, corresponding to 0.5%, 1.0% and 1.5% $O_2$.

The catalyst used in the experiments was a nickel catalyst supported by alumina (13 wt%) and silica (12 wt%). The weight percentage of nickel was 65%. To compare with the nickel catalyst, kieselguhr, a powder material, whose amorphous silica composition is over 95 wt%, was used as a control to study the plasma effect without the presence of a metal catalyst. More detailed information regarding the catalyst material can be found in [11].

A schematic of the plasma system is shown in figure 1. The APPJ was integrated in a high temperature reaction chamber (HVC-DRM-5) by a lab-made macro feedthrough, which was fixed on one of the three viewports [16]. In addition to the feed gas flown through the APPJ, 2 sccm $CH_4$ carried by 400 sccm Ar was injected downstream of the APPJ near the catalyst bed. At this location, the methane and reactive species generated by the APPJ, can interact with each other and with the catalyst through which the gases left the reaction chamber. The quartz tube-to-catalyst distance was fixed at 5 mm for all experiments performed in this work. This distance enabled a relatively large amount of reactive species to arrive at the catalyst surface and allowed a large range of power changes without the plume touching the catalyst and generating arcing. Note that varying the plasma-to-catalyst distance is expected to change certain aspects of the results reported here (see [11]), but this characteristic is not dealt with in this work. The methane and gas products produced from the plasma-catalyst interaction entered a lab-made gas cell with

a 15 cm optical path length sealed with two ZnSe windows, where real-time gas phase characterization was performed using an FTIR spectrometer (IRTracer-100, Shimadzu) equipped with a liquid nitrogen-cooled Mercury-Cadmium-Telluride (MCT) detector. All the gas phase characterizations were done at 0.5 $cm^{-1}$ resolution, Happ-Gentzel apodization and with 10 scans averaged to reduce the baseline noise and improve accuracy. Operando DRIFTS measurements were performed to characterize the catalyst surface. In DRIFTS, the infrared beam passes through KBr windows installed on two viewports of the dome and is scattered off the catalyst surface. The IR beam is then reflected by mirrors in the DRIFTS accessory (Praying Mantis, Harrick Scientific) towards the spectrometer detector. IR spectra showed peaks corresponding to CO, $CH_n$ and other oxygenates, and their intensities were analyzed. Details of the DRIFTS setup and characterization can be found in [16].

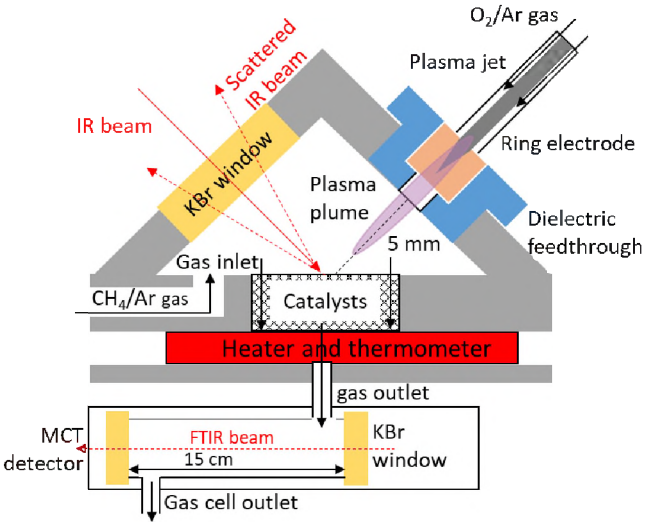


**Figure 1.** The scheme of the reactor for plasma-catalyst interaction and DRIFTS and downstream FTIR measurements. The figure was modified based on the one shown in [16].

The gas lines were evacuated to $10^{-5}$ torr before each experiment, and the reaction chamber was purged by Ar flow to eliminate ambient $CO_2$ and water vapor that cannot be differentiated from

the products of the reactions. During the experiments, the plasma power was increased in steps to the highest possible power without arcing. The plasma treatment time was 5 minutes at each power level which is long enough for the reactions to reach steady state. Both measurements with the catalyst bed at 25 $^{o}$C and heated to 500 $^{o}$C were performed. The catalyst was thermally activated around 360 °C without plasma. However, at this temperature, the thermal catalysis was weak, and the plasma effect still dominated over the thermal effect and the plasma-catalysis synergy effect was weak. At 500 °C, the thermal catalysis plays an important role and can convert a relatively large amount of $CH_4$ gas. For the high temperature experiments, the catalyst was heated at a rate of 10 $^{o}$C/min. When it reached 500 $^{o}$C, pure thermal catalytic reactions were first recorded as a baseline before the APPJ was ignited. Temperature-programmed experiments have also been performed to investigate the plasma effect on the activation energy of the reactions. In these experiments, the plasma was either on or off through the entire temperature ramping process.

The plasma-produced reactive species flux was measured at 5 mm from the nozzle, corresponding to the location of the catalyst bed, with MBMS. The sampling occurred through an orifice of 30 μm in a stainless-steel substrate. More details of the measurement procedure can be found in [31, 35]. As the plasma jet was not in direct contact with the catalyst nor the substrate, the species production in the plasma are independent of the material of the sampling substrate.

## 3. Results

### 3.1. Real-time downstream gas phase characterization

Typical FTIR spectra obtained for a 0.5% $O_2$/Ar flow with and without plasma and at a catalyst temperature of 25 °C and 500 °C are shown in figure 2. Due to the large disturbance of water vapor from ambient environment, water, a possible product of the oxidation of methane, was not quantitatively investigated in this work. The other three species, $CH_4$, CO and $CO_2$, all show IR absorption features that could be related to their density by Beer's law. It should be stressed that the background spectra were taken after the $CH_4$ flow was applied, which is why the consumption of $CH_4$ leads to a negative absorbance.

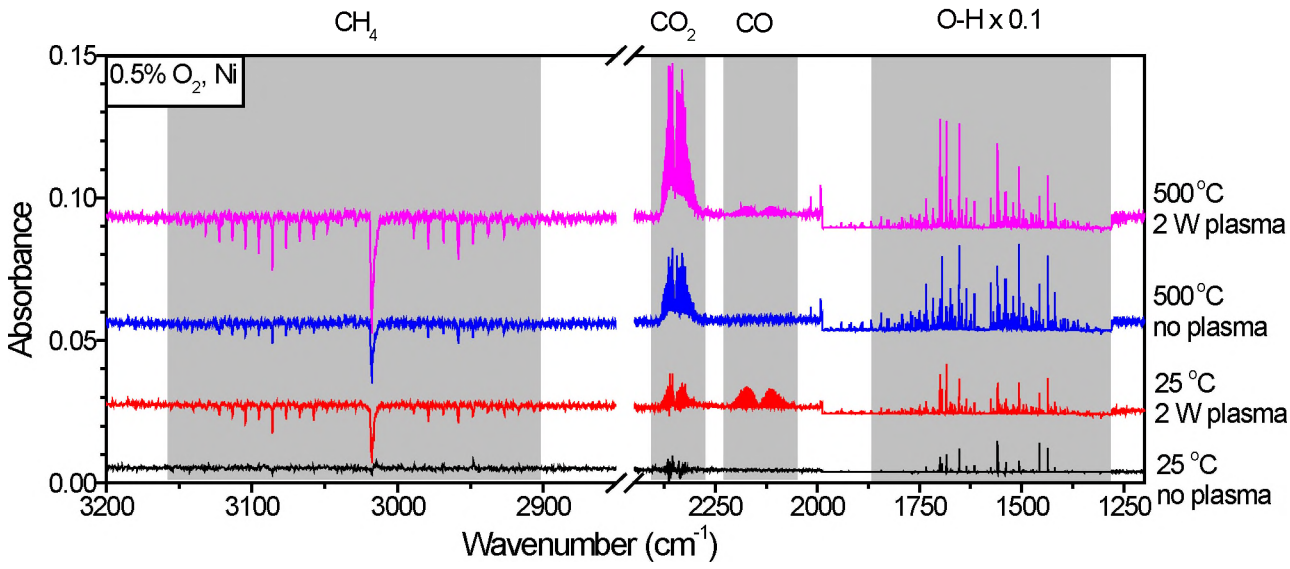


**Figure 2**. Overview of the gas phase FTIR spectra with a feed gas composition of 0.5% $O_2$ in 200 sccm Ar with catalyst temperature of 25 °C without plasma (black), 25 °C with plasma (red), 500 °C without plasma (blue), and 500 °C with plasma (purple).

The IR spectrum recorded at 25 °C without plasma (black spectra) has no $CH_4$ and CO absorption features, consistent with neither $CH_4$ is consumed, nor CO is generated. Nonetheless some $CO_2$ features can be observed due to fluctuation in the ambient $CO_2$ density in the IR beam path, but the average density calculated from those features remains negligible (~$10^{13}$). When the

APPJ was switched on with the catalyst at 25 °C (red spectra), $CH_4$, CO and $CO_2$ features readily appeared, indicating that the oxidation of $CH_4$ to both CO and $CO_2$ was taking place. With the catalyst at 500 °C without plasma (blue spectra), thermal catalytic reactions did not produce CO gas but the $CH_4$ was undergoing complete oxidation to $CO_2$. When the plasma was switched on with catalyst at 500 °C (purple spectra), a drastic increase of $CH_4$ consumption and $CO_2$ generation could be seen, while CO absorption bands have a lower intensity than that at 25 °C.

The IR absorbance of $CH_4$, CO and $CO_2$ were converted to number density (number/$cm^3$) based on Beer's law, which is shown in the following equation:

$$n = \frac{Abs}{0.4343 * \sigma * l} \qquad (1)$$

In this equation, $n$ is the density of the gas calculated from a certain absorption peak, $Abs$ is the absorbance measured by FTIR at that peak, $\sigma$ is the attenuation cross section, which is calculated from the HITRAN FTIR database [36], and $l$ is the optical path length of the gas cell which is 15 cm [16]. To calibrate the gas density, a known amount of $CH_4$, CO or $CO_2$ was flowed through the gas cell. The measured density was found to be linearly proportional to the real concentration, and a correction factor for each gas was obtained by comparing the real density with the measured density, which was 2.789, 0.46 and 0.19 for $CH_4$, CO and $CO_2$, respectively. Details of the gas quantification method can be found in [16].

### 3.1.1. Variation of plasma power, $O_2$ flow rate and catalyst temperature

The concentration of consumed $CH_4$, generated CO and $CO_2$ at a catalyst temperature of 25 °C and 500 °C as a function of the plasma dissipated power is plotted in figure 3. In general, increasing the plasma power can enhance the $CH_4$ consumption and CO and $CO_2$ production, which is due to the increase of plasma density, reactive species fluxes and plasma plume length.

Conversely, increasing the $O_2$ flow rate lowers the $CH_4$ conversion at the catalyst temperature of 25 $^oC$, as the reactive species density and plasma plume length are reduced upon the addition of $O_2$ gas [37]. However, at 500 $^oC$ in the thermal-driven dominant region (low plasma power), the $O_2$ flow can increase the $CH_4$ consumption (figure 3b) and $CO_2$ production (figure 3f) due to the enhancement of thermal reaction. Note that although the error bar for the $CO_2$ production is relatively large due to the disturbance from the ambient $CO_2$, figure 3f still shows the increase of $CO_2$ generation due to the enhanced thermal catalytic reaction induced by the increased $O_2$ gas at low plasma power region. As for CO, it can only be generated at significant quantities in the presence of plasma for the investigated conditions in this work and the increase in $O_2$ addition did not enhance CO production even with the catalyst at 500 $^oC$. In addition, we found that the $CH_4$ consumption and $CO_2$ production are enhanced at a catalyst temperature of 500 $^oC$ compared to 25 $^oC$ while the CO production reduces. In this work, the conversion rate of $CH_4$ to CO and $CO_2$ is around 90%, which indicates that the formation of other byproducts is not significant. However, less than 10% of the overall methane was oxidized, which was much lower compared to flowing methane through the plasma source [9], because of less direct interaction between the ionizing plasma and the methane.

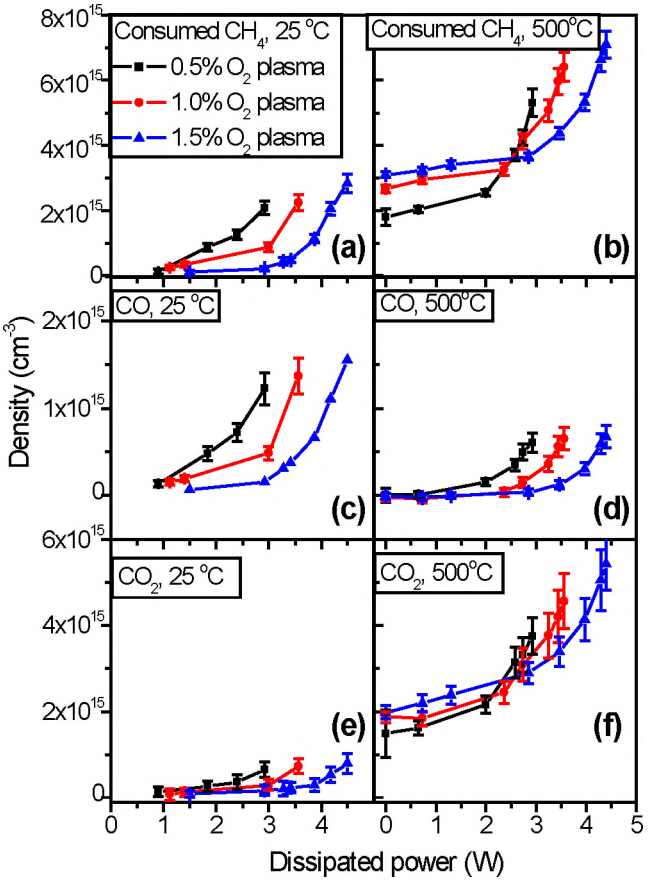


**Figure 3.** Measured densities of CO, $CO_2$ and $CH_4$ under various plasma powers at a catalyst temperature of 25 °C or 500 °C: $CH_4$ consumption at 25 °C (a) and 500 °C (b), CO production at 25 °C (c) and 500 °C (d), and $CO_2$ production at 25 °C (e) and 500 °C (f).

### 3.1.2. Temperature-programmed experiments

To evaluate the effect of plasma on the activation energy, temperature-programmed experiments were performed with and without plasma application. The nickel catalyst was continuously heated from 25 °C to 500 °C at 10 °C/min with 1 W plasma jet. Downstream gas-phase measurements were recorded throughout the entire temperature-ramping process. As shown in figure 4a, the consumption of $CH_4$ is an activated process that is enhanced with temperature.

Without plasma, the nickel catalyst was activated at 360 $^{o}$C, as indicated by the temperature where the consumption of $CH_4$ started to increase. With 1 W plasma, the activation temperature was lowered to 310 $^{o}$C. It is worth noting that the gas temperature of a 1 W plasma was measured to be ~310 K, hence the heating due to the plasma was negligible [38].

As we have seen in figure 3, CO production becomes weaker while the $CO_2$ production is boosted at a catalyst temperature of 500 $^{o}$C than at 25 $^{o}$C, one may speculate that CO is oxidized to $CO_2$ at elevated catalyst temperature. We conducted an experiment to evaluate the temperature evolution of CO and $CO_2$. The plasma power was set at a relatively high value (3 W) in order to enhance the plasma-catalyst interaction. In figure 4b, the CO curve starts to decline at around 200 $^{o}$C, while the $CO_2$ curve begins to increase at the same temperature. This result clearly demonstrates that $CO_2$ is favored at high temperature. It is worth noting that the amount of decreased CO cannot compensate for the amount of increased $CO_2$ since the $CO_2$ production at high temperature with plasma also includes the thermal catalysis and other synergistic effects that can enhance the reaction. We also found that heating of the catalyst does not cause noticeable change of the plasma properties (shown in figure 9), the oxidation of CO to $CO_2$ should happen on an activated catalyst surface.

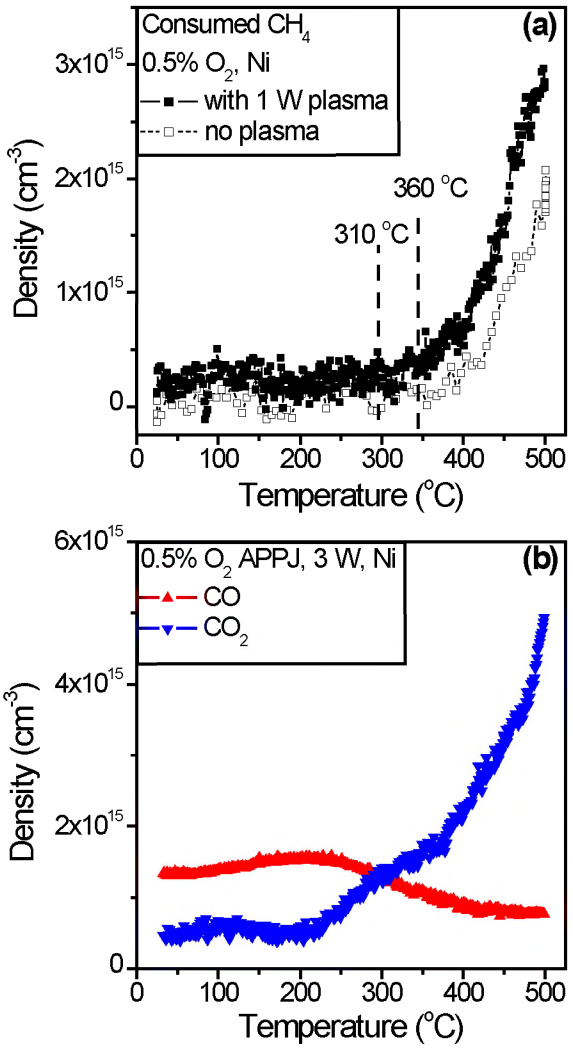


**Figure 4.** (a) The temperature dependence of $CH_4$ consumption with and without the 1 W $Ar/O_2$ plasma. (b) Density profile of CO and $CO_2$ as a function of temperature using 3 W $Ar/O_2$ plasma. The catalyst was heated from 25 °C to 500 °C at 10 °C/min.

### 3.2. Reactive oxygen species

The most dominant ROSs produced by $Ar/O_2$ APPJ are atomic oxygen, ozone and singlet oxygen, and their density profile measured by MBMS was shown as a function of dissipated plasma power in figure 5. The variation of the atomic O density exhibits a similar trend with plasma power as the consumed $CH_4$ and produced CO and $CO_2$ densities do, while $O_3$ and

singlet $O_2$ do not have similar correlation. We have correlated the fluxes of atomic O and gas phase species from the $CH_4$ conversion reactions and is discussed in 4.2. For additional information regarding the ROSs produced by the APPJ, the reader can refer to [31, 34].

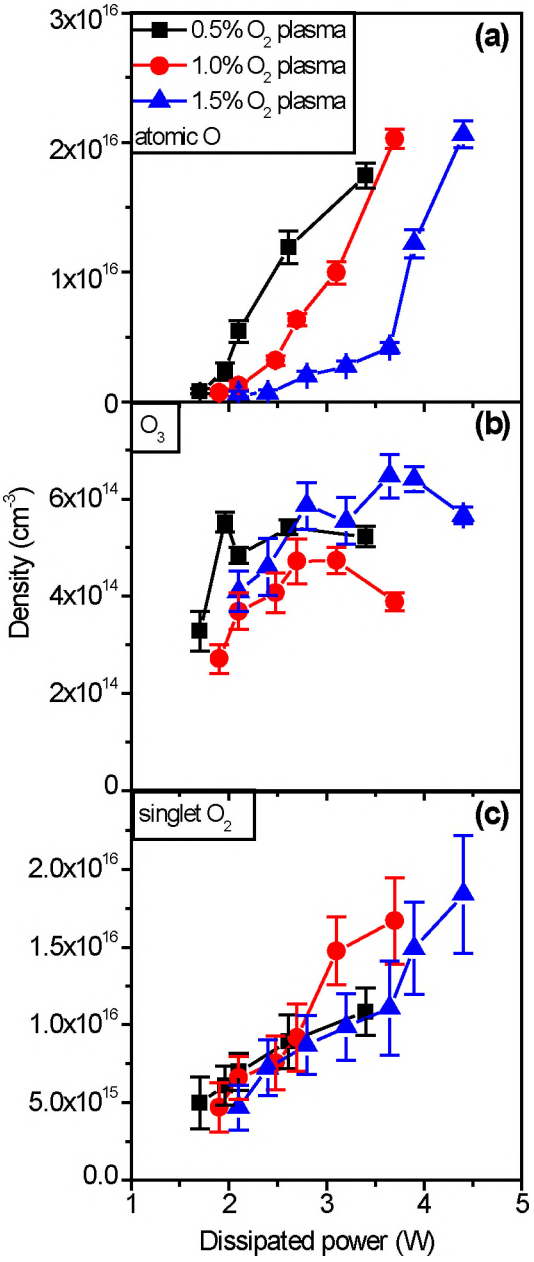


**Figure 5**. The ROSs densities at a distance of 5 mm from the APPJ nozzle as a function of plasma power [31, 35].

### 3.3. DRIFTS results

The evolution of surface species on the catalyst was measured in-situ by the DRIFTS cell integrated into the FTIR sample compartment. The experimental conditions and plasma treatment procedure were the same as for the downstream gas phase measurements so that complementary gas phase and surface data could be obtained. The FTIR was set at 4 $cm^{-1}$ resolution, Happ-Gentzel apodization and with 20 scans averaged for the DRIFTS measurements. Background spectra were taken using a pristine catalyst sample. Thus, a positive signal in the DRIFTS measurements indicates the formation of surface species, whereas a negative signal means a loss of surface species. While no quantitative analysis of the DRIFTS measurements were attempted, the changes in relative absorbance in the DRIFTS spectra is still qualitatively related to the abundance of the surface species [39].

Figure 6 shows a selection of DRIFTS spectra for catalysts at 25 $^{o}$C and 500 $^{o}$C with or without a 2 W plasma jet with 0.5% $O_2$. The band observed around 3500 $cm^{-1}$ is associated with hydroxyl groups [40]. The hydroxyls can be derived from either the chemical reactions, or the water vapor residues inside the reactor and gas tubing. $CH_4$ peaks at 2900 to 3150 $cm^{-1}$ and around 1300 $cm^{-1}$ [41] can be observed. However, these peaks are due to changes in gas phase $CH_4$ rather than surface-adsorbed $CH_4$. This was confirmed by DRIFTS measurements after the plasma treatment and flushing of the reactor that led to the immediate disappearance of the $CH_4$ absorption features, while surface species typically remain on the surface longer and retained their absorption features. Similarly, gas phase absorption can be observed for $CO_2$ around 2280–2290 $cm^{-1}$ [42, 43]. The origin of these gas phase absorptions was from the IR light going through the gas phase above the catalyst before and after it was scattered on the surface.

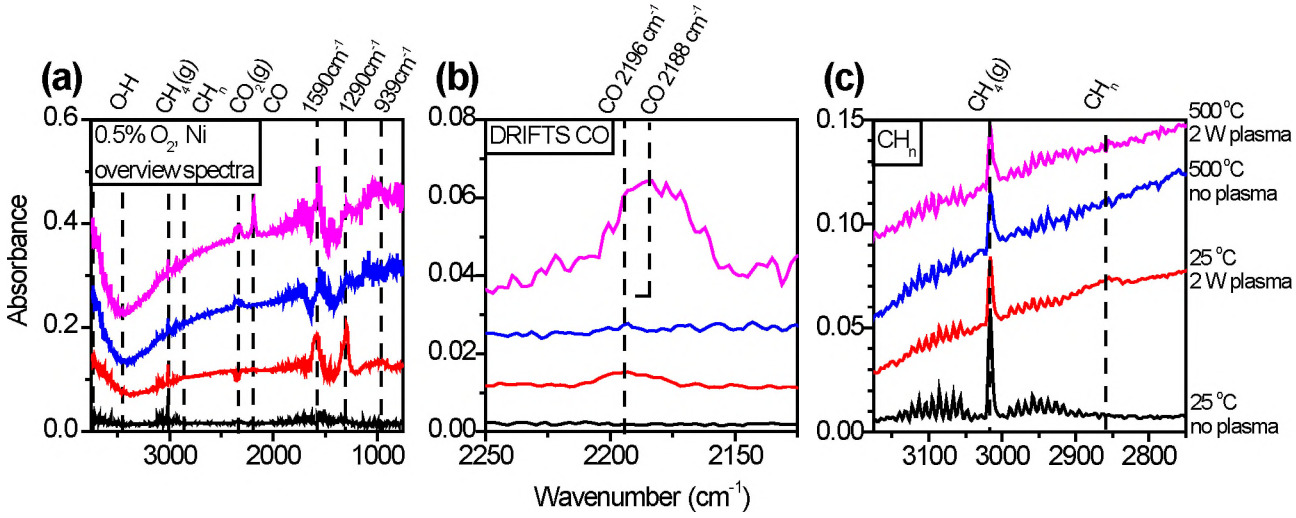


**Figure 6.** The DRIFTS spectra with or without the 2 W plasma jet with a gas composition of 0.5% $O_2$ in 200 sccm Ar at a catalyst temperature of 25 °C and 500 °C: 25 °C no plasma (black), 25 °C with plasma (red), 500 °C no plasma (blue), and 500 °C with plasma (purple). (a) An overview of DRIFTS spectra. (b) Magnified spectra of the surface CO. (c) Magnified spectra of the surface $CH_n$ and gas phase $CH_4$.

For a catalyst sample at 25 °C without plasma, other than O-H and gas phase $CH_4$ peaks, no other IR peaks are observed. When the 2 W APPJ was applied on the 25 °C catalyst, a surface CO absorbing at 2196 $cm^{-1}$ [11] and surface $CH_n$ absorbing at 2860 $cm^{-1}$ [41, 44] was observed, as shown in figure 6b and 6c by the red spectra. Unfortunately, the IR bands of $CH_n$ (n=1, 2 and 3) overlap in the range of 2800-3100 $cm^{-1}$ in our experiment [45], and unambiguous assignment of the peaks to a specific $CH_n$ species is difficult, thus we refer to the band at 2818–2914 $cm^{-1}$ as $CH_n$ in general. For a catalyst at 500 °C without plasma, no surface CO or $CH_n$ peaks were observed as shown by the blue spectra in figure 6, which is consistent with the gas phase results that no CO and only $CO_2$ is produced at 500 °C without plasma (figure 2). After the APPJ was switched on at 500 °C, a strong surface CO peak at 2188 $cm^{-1}$ was observed. No surface $CH_n$ was

observed at this condition, which is a distinctive difference with the 25 °C catalyst case. In figure 6b, the vibrational frequency of CO shows a blue shift from the gas phase free CO molecule (2143cm$^{-1}$, figure 2) to surface-adsorbed CO at 25 °C (2196 cm$^{-1}$) and 500 °C (2188 cm$^{-1}$). This is likely due to the oxidation state of nickel and will be discussed in 4.4.

The other absorption features present in the DRIFTS spectra at 1590 cm$^{-1}$, 1290 cm$^{-1}$, and 939 cm$^{-1}$ can be assigned to carboxylate [41, 46], carbonate [47], and superoxo or nickel oxide [48], respectively. The unambiguous assignment of the peaks between 750–1800 cm$^{-1}$ is hard, as many species, such as carbonate, carboxylate, hydroxyl, etc. with overlapping absorption bands are located in this range. Additionally, the absorbance of these species seems independent of the plasma power, as shown in figure 7. In the scope of this work, it is possible that those species act as spectator species or mild intermediates that do not play a key role in the reactions, as discussed by Demoulin et al. [42] and Meunier et al. [49] in their work. Further investigation of those species is outside the scope of this work.

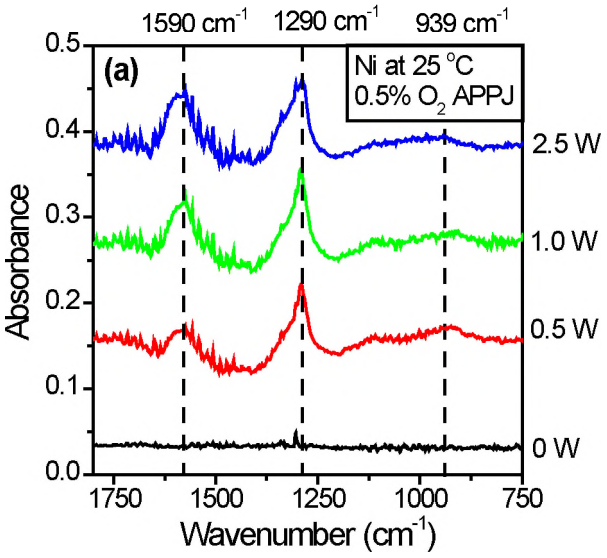

**Figure 7.** DRIFTS spectra in the region of 750-1800 $cm^{-1}$ at the catalyst temperature of 25 °C. The APPJ feed gas was 0.5% $O_2$ in 200 sccm Ar, and different powers were selected. Three main absorption features from surface species at 1590, 1290 and 939 $cm^{-1}$ might be assigned to carboxylate, carbonate and $O_2^-$ ions or nickel oxide, respectively.

## 4. Discussion

### 4.1. Effects of $O_2$ additives on decomposing $CH_4$

Figure 8a shows that increasing the $O_2$ admixture to $Ar/O_2$ feed gas decreases the consumption of $CH_4$ at 25 °C. The addition of $O_2$ to the plasma source leads to the quenching of high-energy electrons, metastable species and reactive oxygen species [37, 50-52], resulting in the decrease of plasma-induced reactivity. The plasma plume length also decreases significantly upon increasing $O_2$ addition [52]. The correlation between plume length and conversion has two origins: the stronger mixing of the surrounding $CH_4$ with the ionizing plasma in the case of the larger plume length or the distance short-lived radicals that are rapidly decaying afterglow have to travel. In addition, the lifetime of, for instance, the O radical is strongly impacted by the $O_2$ concentration as its main destruction pathway is through the recombination with $O_2$ forming $O_3$ in a three body reaction [32]. Hence, the $O_2$ concentration could drastically impact O flux to the catalytic surface and reduce the $CH_4$ conversion.

At a catalyst temperatures of 500 °C, an increased amount of $O_2$ can promote the consumption of $CH_4$ in thermal-driven catalytic reactions as shown in figure 8b [53]. This process seems to favor $CH_4$ to $CO_2$ conversion. This conclusion remains valid in plasma catalysis with low plasma power, where the dominant reaction is still the thermal-driven catalytic reaction. With increasing plasma power, however, the plasma-induced effects become more pronounced and a similar reduction in $CH_4$ conversion with increasing $O_2$ addition occurs. The transition point between

these two different trends is 2.5 W. At this power, $CH_4$ conversion is independent of the amount of $O_2$ added to the feed gas.

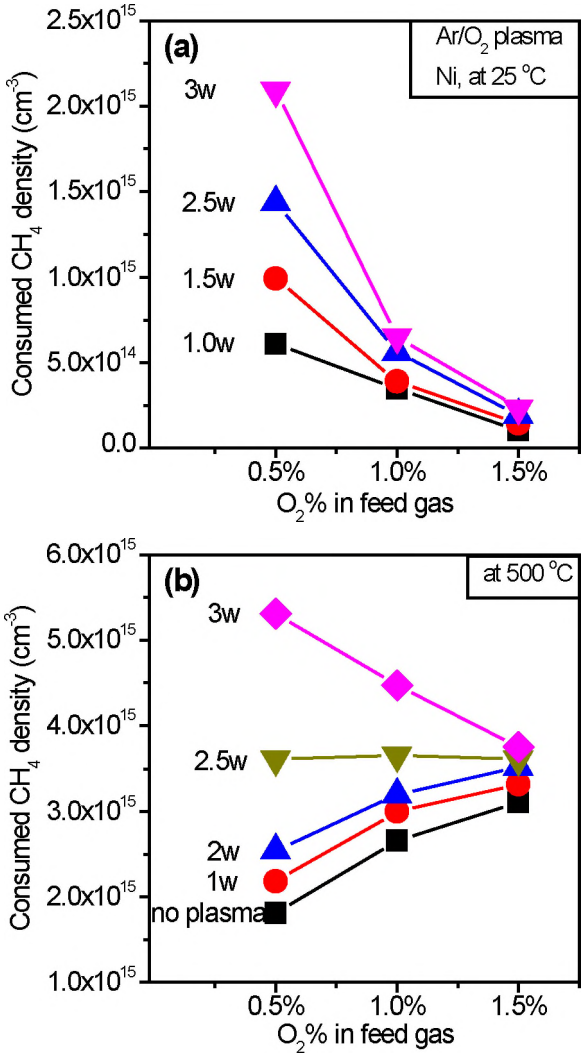


**Figure 8.** $CH_4$ consumption for different $O_2$ amounts in the feed gas at different plasma powers at a catalyst temperature of 25 °C (a) and 500 °C (b). As a reference, no plasma conversions have also been included. The data are extracted from figure 3.

### 4.2. Role of atomic O

#### 4.2.1. Validity of using MBMS fluxes to correlate with conversion

Before looking in more depth to correlations between plasma-produced ROSs and $CH_4$ conversation, it is crucial to assess whether heating of the catalyst bed impacts plasma conversion. To this end, we replaced the catalyst with kieselguhr powders treated by plasma and assessed the $CH_4$ conversion at a kieselguhr powder temperature of 25 $^oC$ and 500 $^oC$ without the presence of a metal catalyst as shown in figure 9. No significant difference in $CH_4$ conversion was observed confirming that the heating of the catalyst bed to 500 $^oC$ has a negligible effect on the methane conversion.

As the catalyst particles were loosely packed in the holder, the effluent of the plasma jet could easily flow through the catalyst holder without much flow resistivity in the experiments. The convection timescale over a distance of 1 mm when approaching the catalyst bed is estimated to be ~1.7 ms, based on the gas velocity entering the catalyst holder. When the catalyst temperature increases from 25°C to 500°C, the convective transport of reactive species to the catalyst holder is not impacted significantly. This is because the timescale of thermal diffusion is estimated to be on the order of ~45 ms over a distance of 1 mm (based on $l^2/\alpha$, $l$ is the characteristic length and $\alpha$ is the thermal diffusivity of Argon 2.2 $\times 10^{-5}$ $m^2$ $s^{-1}$), which is much longer than the corresponding convection timescale (~1.7 ms). Therefore, the convection is more dominant over the heat diffusion and there is negligible temperature gradient in the upstream gas phase before the catalyst holder. Hence the plasma produced reactive species fluxes measured at 25°C are representative for both the catalyst operating at 25°C and 500°C. Note however, that this estimate implies that the thermal gradients occur in the catalytic bed and the given temperatures should be interpreted as holder temperatures during the application of the gas flow.

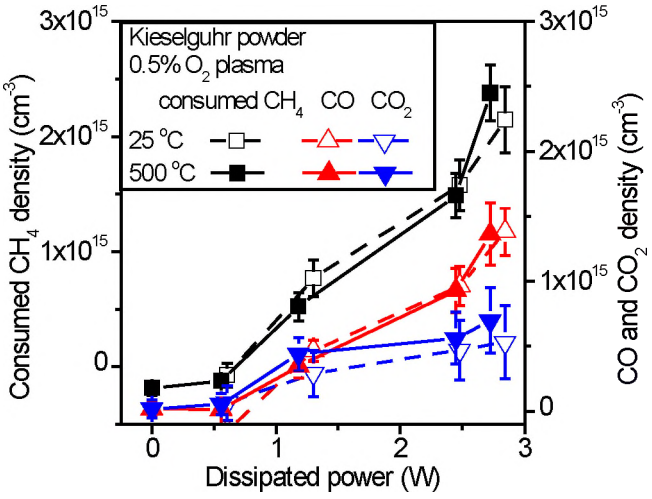


**Figure 9.** $CH_4$ density as a function of plasma power with kieselguhr powder instead of catalyst at a temperature of 25 °C and 500 °C.

### 4.2.2. Correlation between $CH_4$ conversion and atomic O flux

To evaluate the effect of the ROSs produced in the plasma, we converted the measured density ($cm^{-3}$) to flux ($cm^{-2}s^{-1}$) on the catalyst surface at a distance of 5 mm from the quartz tube. As the gases flow through the catalyst bed (and in the case of the MBMS similarly gas suction into the sample orifice occurs) the catalyst surface is not a stagnation zone and the flux can be estimated from the local gas velocity and density as the species are convectively transported into the catalytic bed.

$$\Gamma = \frac{\rho Q}{A} \qquad (2)$$

Here $\Gamma$ is the average particle flux ($cm^{-2}s^{-1}$), $\rho$ is the gas density ($cm^{-3}$) which can be measured by FTIR for $CH_4$, CO and $CO_2$, and by MBMS for ROSs, $Q$ is the volumetric flow rate ($cm^3s^{-1}$), $A$ is the catalyst bed cross section ($cm^2$). While we recognize that in this system concentration

gradients will be present due to mixing of the feed gas through the jet and gas added in the chamber, a first order estimate of the gas velocity at the catalytic bed can be obtained by expressing mass conservation of the gas flow through the system.

By correlating the ROSs and the consumed $CH_4$, and produced CO and $CO_2$ fluxes, we found that atomic O flux exhibits a linear correlation with the fluxes of consumed $CH_4$ and produced CO and $CO_2$, as shown in figure 10. However, the other two ROSs, singlet oxygen and ozone, do not show any obvious correlation. The flux of the consumed $CH_4$, produced CO and $CO_2$ is proportional to the atomic O flux delivery to the catalytic bed, and the curves coincide for all $O_2$ flow rates at a catalyst temperature of 25 $^oC$. As the ion flux and UV flux are very small for these jet conditions [50, 54], these observations are consistent with the hypothesis that atomic O is the key reactive species that contributes to the reaction. Luan et al. [55] studied polymer etching using a similar APPJ, and they found that the etching depth of the polymers mirrors the flux of atomic O produced from the APPJ, and a similar proportional relationship between the etching depth and atomic O flux was established. They concluded that the atomic O initiates and directly participates in the polymer etch [55] which was confirmed by a detailed quantitative analysis involving a broader range of radical species in [56]. In addition, at a catalyst temperature of 500 $^oC$, the enhancement of the $O_2$ flow on thermal conversion of $CH_4$ to $CO_2$ is reflected in figure 10, indicating that the thermal catalytic reaction utilizes $O_2$ gas to oxidize $CH_4$.

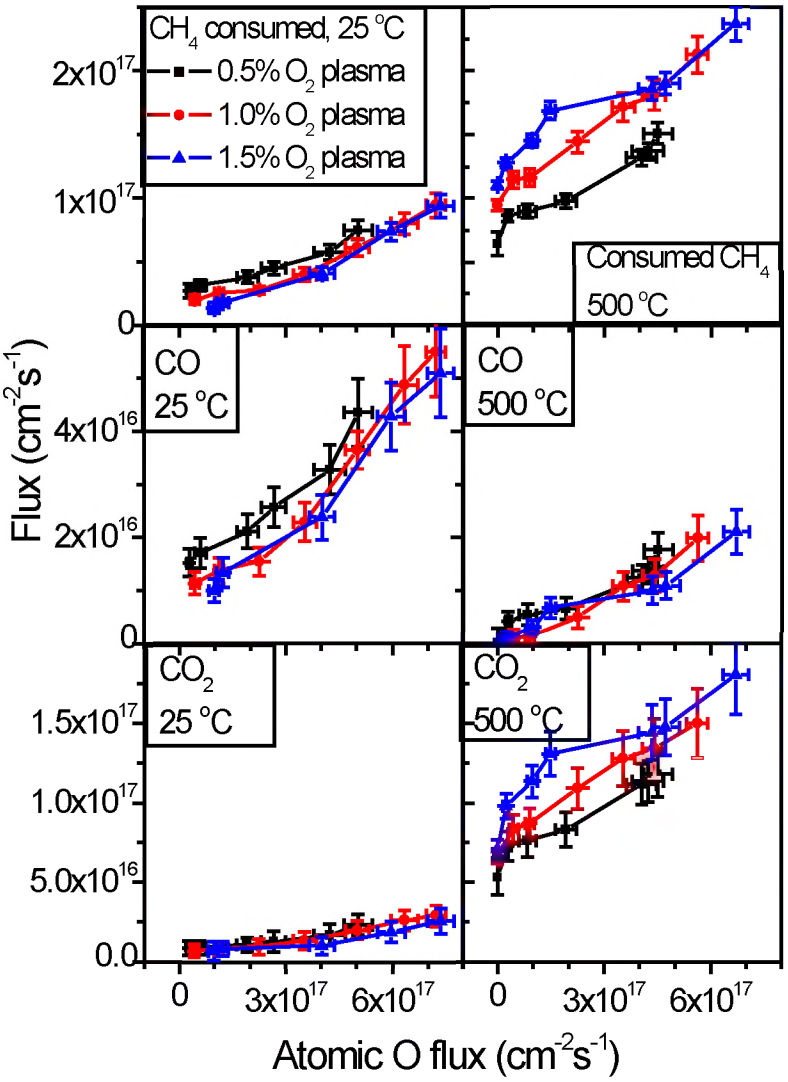


**Figure 10.** Correlation between the fluxes of consumed $CH_4$, produced CO and $CO_2$ and atomic O at the catalyst temperature of 25 °C (a) and 500 °C (b). The concentration of $CH_4$, CO and $CO_2$ was extracted from figure 3, and that of atomic O was extracted from figure 5. The fluxes of the gases and atomic O were calculated based on Eq. (2).

### 4.3. Apparent activation energy and synergistic effect

Based on the temperature dependence profile of $CH_4$ consumption in figure 4a, the apparent activation energy can be calculated through the rate equation and Arrhenius equation:

$$r = K[CH_4]^a[O_2]^b \quad (3)$$

$$K = A \cdot e^{-\frac{E_a}{RT}} \quad (4)$$

Here $r$ is the $CH_4$ consumption rate, which is calculated by multiplying the concentration of consumed $CH_4$ by the total flow rate, $K$ is the reaction rate coefficient, $a$ and $b$ represent the reaction order for $CH_4$ and $O_2$ respectively, $E_a$ is the apparent activation energy, and $T$ is the temperature of the reaction. By combining the two equations, the apparent activation energy can be extracted from the slope of $CH_4$ consumption rate vs. $1/T$.

$$\ln(r) = \ln(a) + a \cdot \ln[CH_4] + b \cdot \ln[O_2] - \frac{E_a}{R}\frac{1}{T} \quad (5)$$

The log of the reaction rate is linearly proportional to $1/T$ with $-E_a/R$ as the slope. Figure 11 is the log of $CH_4$ consumption rate as a function of $1000/T$. The apparent activation energy is calculated to be 81.86 kJ/mol (0.85 eV) for the thermal catalytic reaction, and 47.86 kJ/mol (0.50 eV) for the plasma-enhanced catalysis reaction, based on the linear fit of the Arrhenius plot as shown by the dashed (no plasma) and solid (with 1 W plasma) lines in figure 11. A decrease in apparent activation energy of over 40% is observed. Geng et al. investigated the methane catalytic combustion over a Cu catalyst, and the apparent $E_a$ was found to be around 100 kJ/mol, depending on the $O_2/CH_4$ ratio [57]. The discrepancy of measured apparent $E_a$ between their work and ours could be due to the difference of the setup as well as the catalyst used. Unfortunately, we did not find any literature that includes the calculation of the apparent $E_a$ for the oxidation of $CH_4$ by $Ar/O_2$ plasma.

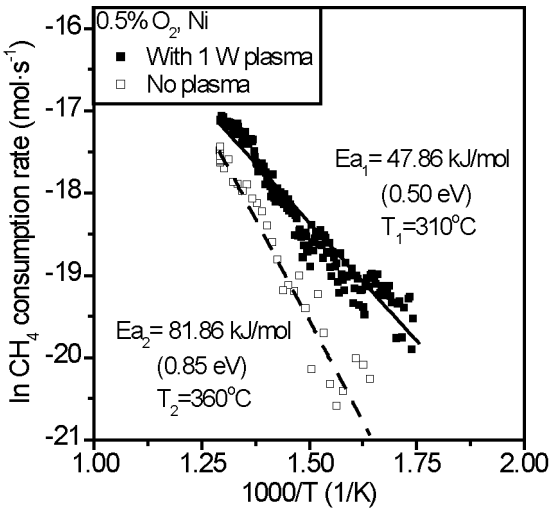


**Figure 11.** The Arrhenius plot of $CH_4$ consumption with and without the 1 W $O_2$/Ar plasma. The data was calculated from figure 4a based on Eqs. (3)–(5).

The plasma can dissociate $CH_4$ and $O_2$ to reactive intermediates, such as $CH_n$ for $CH_4$ (see supplementary material for the discussion of $CH_4$ dissociation by plasma-produced species) and atomic O for $O_2$. The plasma can also generate vibrationally excited methane ($CH_{4\_vib}$) which can be dissociated on active catalyst sites with less energy input [58], although this is less likely in the present study as the $CH_4$ is not fed through the ionizing plasma. The contribution of the plasma lowers the apparent activation energy required to break down the strong chemical bonds that usually require high temperatures [58]. At the catalyst temperature of 500 °C with the APPJ, more reactive species participate in the chemical reactions on the surface than without plasma, which contributes to the synergistic effect in plasma catalysis. As can be seen in figure 12, the catalytic reaction with 1.0% $O_2$ plasma at 500 °C consumes more $CH_4$ (31% higher using 3.5 W APPJ) than is consumed if one combines the separate reactions of plasma at 25 °C (pure plasma effect, catalyst was not active) and pure thermal catalysis at 500 °C (no plasma). The sum of CO

and $CO_2$ products using the 1.0% $O_2$ APPJ at 500 °C catalyst temperature is also higher than the sum of the separate reactions (32% higher using 3.5 W APPJ). Therefore, a synergy of about 30% can be observed in our system. Nonetheless, the temperature increase at the catalyst bed can extend the lifetime of the O radical as the dominant recombination reaction is highly sensitive to temperature [32]. However, the influence of the increased O radical lifetime on the $CH_4$ conversion at elevated catalyst temperature is out of the scope of this paper and will not be discussed in this work.

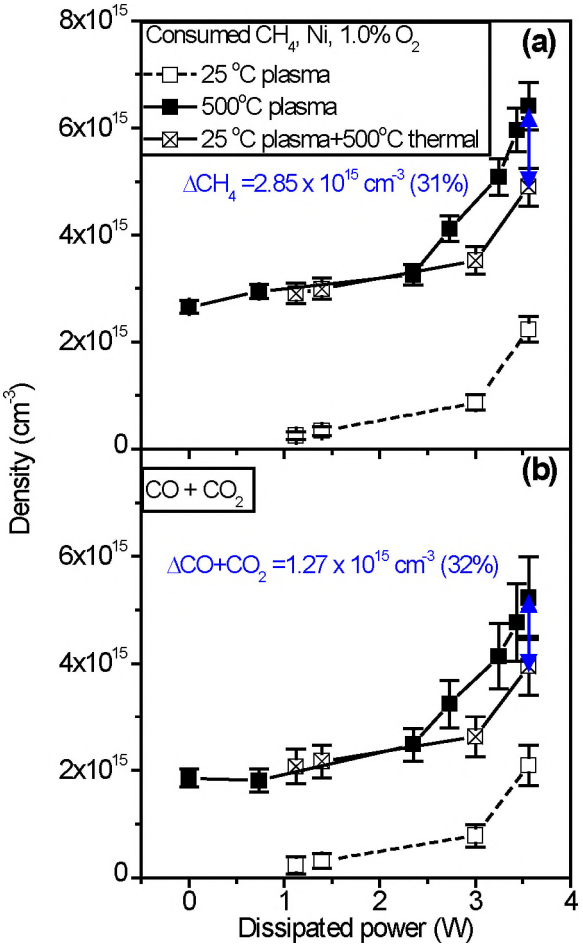


**Figure 12.** Comparison of plasma catalysis at 500 °C using 1.0% $O_2$ in an APPJ with the sum of using an APPJ at 25 °C and pure thermal catalytic reaction at 500 °C. Plasma catalysis at 500 °C (a) consumes

more $CH_4$ and (b) generates more products (sum of CO and $CO_2$) than the combination of the other two cases.

### 4.4. Changes of CO vibrational frequency

One important observation is that the CO IR vibrational frequency shifts from that seen for the CO molecule in the gas phase when a surface-adsorbed species is studied. As shown in figure 13, the free gas CO measured by downstream FTIR has absorbance bands centered at a wavenumber of 2143 $cm^{-1}$, in agreement with literature [36]. The surface-adsorbed CO measured by DRIFTS at 25 $^{o}C$ catalyst temperature has an absorbance blue shifted by 53 $cm^{-1}$ from the free gas CO frequency. This phenomenon is consistent with simulations by Politzer et al [59]. Politzer et al. attributed the frequency increase of surface-adsorbed CO to the net transfer of charge from the carbon to Ni. Upon the formation of Ni-CO structure, CO could transfer its $\sigma$ electrons to the Ni surface, while gaining antibonding $2\pi^*$ electrons from the Ni surface [60]. The loss of the $\sigma$ electrons is larger than the gain of the antibonding $2\pi^*$ electrons if the CO is bonded to positively charged Ni ions, for instance, in nickel oxide, resulting in a stronger C-O bond and giving rise to a higher vibrational frequency. Spectroscopic studies of surface-adsorbed CO also showed that CO bonded to oxide surfaces displays a blue shift from its free gas component [61-63]. Lu et al. found a shift of surface-adsorbed CO bands to higher wavenumber, and they explained such phenomenon by the decrease of electron density on platinum, which was caused by the attraction of electrons from surface oxygen species [63].

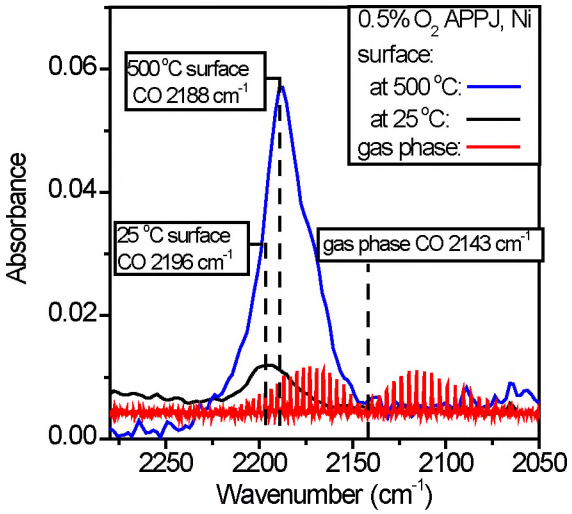


**Figure 13.** IR spectra of gas phase CO (red) and surface CO at 25 °C (black) and 500 °C (blue). The surface CO exhibits a blue shift from the gas CO (2143 $cm^{-1}$). The surface CO at catalyst temperature of 500 °C shows a red shift from that at 25 °C.

The catalyst temperature also plays a role in determining the IR frequency of surface CO. When the catalyst temperature goes up to 500 °C, the surface CO shows a wavenumber at 2188 $cm^{-1}$, which still exhibits a blue shift from the gas phase CO, but the frequency is slightly lower than that of the surface CO at a catalyst temperature of 25 °C. According to the work described in [64], $CH_4$ could interact with the lattice O in the catalyst to form $CO_2$. Replenishing lattice O may not be fast enough, and thus a relatively more reduced nickel catalyst can be produced at 500 °C than at 25 °C. The extent of charge transfer increases with the positive charge of the Ni ions [59]. At 500 °C, due to loss of surface oxygen, the nickel ions have fewer positive charges on average than for a 25 °C catalyst. Subsequently, less charge transfer between the surface-adsorbed CO and nickel catalyst takes place at 500 °C, and the blue shift of the CO vibrational frequency at the catalyst temperature of 500 °C would be more moderate than that at 25 °C.

### 4.5. Important correlations and possible mechanisms of plasma–assisted catalytic reactions for the $Ar/CH_4/O_2$ system

#### 4.5.1. Analysis of gas phase and surface species with varying plasma power and catalyst temperature

In order to understand the mechanism of the plasma catalysis reactions in our system, we have compared the downstream gas phase measurements with the in-situ surface DRIFTS measurements. The gas phase CO and $CO_2$ data can be directly extracted from figure 3 and is shown on the right y-axis in figure 14. Qualitative analysis of surface CO and $CH_n$ from the DRIFTS data was processed and shown on the left y-axis in figure 14. The absence of surface CO, surface $CH_n$ and gas phase CO in thermal catalytic reactions in our system (shown as 0 W dissipated power in figure 14b) indicates that the gas phase $CH_4$ is oxidized to $CO_2$, possibly by surface O derived from the breakdown of surface-adsorbed $O_2$ over active catalyst-sites, as also suggested by Hu et al. [27, 64, 65]. By using transient response methods, Hu et al. demonstrated that the gas $CH_4$ can directly react with surface-adsorbed oxygen to produce $CO_2$ and suggested that this process possibly follows an Eley-Rideal mechanism [64]. Dissanayake et al. used XPS to analyze the unreduced nickel catalyst surface and did not detect carbon formation on the surface at 500 $^oC$, and they also did not observe the formation of gas CO at 500 $^oC$ [22].

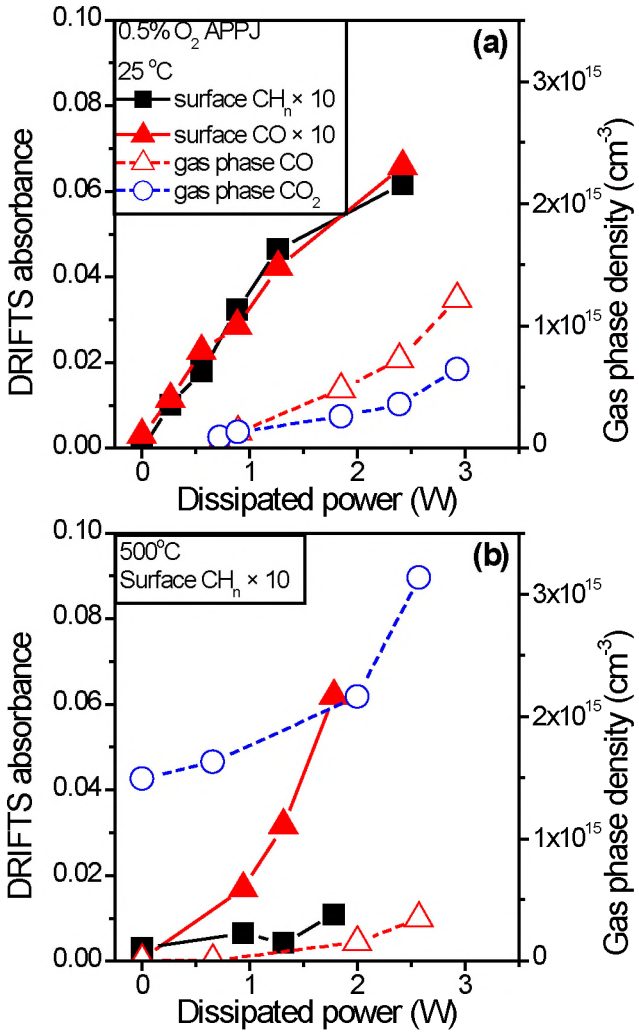


**Figure 14.** Surface $CH_n$ and CO absorbance, and gas phase CO and $CO_2$ densities as a function of plasma power at a catalyst temperature of 25 °C (a) and 500 °C (b). The absorbance of surface CO and $CH_n$ at 25 °C and $CH_n$ at 500 °C was multiplied by a factor of 10 for a clearer comparison.

In figure 14a, it is shown that at 25 °C the surface CO follows the trend of surface $CH_n$ with plasma power. This tight correlation indicates that the surface $CH_n$ is connected with the formation of surface CO. The $CH_4$ can be decomposed by high-energy plasma-produced species and dehydrogenation to $CH_n$, which is adsorbed on the surface and then oxidized by atomic O to CO and $CO_2$. Alternatively, the plasma also may produce vibrationally excited $CH_4$* which can

adsorb on the surface as $CH_n$ [58]. Although the reaction is taking place at the surface at 25 °C as confirmed by the detected surface species, gas phase products can also be generated from the oxidation of adsorbed $CH_n$ on other surfaces by atomic O produced from the APPJ for situations without catalyst and just support. Additionally, we cannot rule out the gas phase formation of CO by direct interactions involving no catalyst site. However, we consider these to be minor reactions and they are not discussed in this work. Knoll et al. [16] demonstrated that the orifice-to-surface distance plays an important role on the acquired results even at a catalyst temperature of 25 °C, and the plasma impacts are much greater for short orifice-to-surface distances. The reason presented is the short lifetime of O atoms which limits the flux of species that can reach the surface, and the surface reactions will mirror the amount of reactive species that arrive at the surface.

When the catalyst temperature was increased to 500 °C, we observed very little absorbance due to surface $CH_n$, while a ten-fold increase of surface CO absorbance was seen as compared to the situation with the catalyst temperature of 25 °C as plasma power was increased (see figure 14b). The large amount of surface CO species observed at 500 °C catalyst temperature is contrary to the temperature characteristics of direct adsorption of CO from the gas phase which should become weaker as temperature increases [66, 67]. This suggests that a fast surface CO production reaction should exist on the activated catalyst surface for plasma operating conditions. We postulate that the surface CO species is derived from the rapid oxidization of surface $CH_n$ at 500 °C driven by incident plasma-produced O, and possibly due to plasma-induced stimulation of interaction with NiO sites. Additionally, thermally driven oxidation of $CH_n$ by surface-adsorbed $O_2$ takes place at 500 °C. The oxygen-related consumption of $CH_n$ on an activated catalyst surface is so rapid that its density remains very low, while the surface CO

density is high. This is consistent with the dominance of $CO_2$ gas production over CO gas production at this condition since surface CO can be further oxidized to $CO_2$ due to the activated catalyst, whereas at 25 $^oC$ such oxidation is less likely to occur. At 500 $^oC$, the transformation of $CH_4$ to surface $CH_n$ might be the rate-determining step of the production of CO and $CO_2$, since the low surface $CH_n$ density limits the reaction rate and the subsequent oxidation proceeds much faster. Nozaki et al. investigated methane steam reforming in a hybrid barrier discharge-catalyst ($Ni/Al_2O_3$) reactor, and they found that the dehydrogenation of methane is the rate-determining step [3]. The activation of $CH_4$ to $CH_n$ can be enhanced by directly flowing $CH_4$ through the APPJ, thus a much higher reaction rate can be achieved. We have investigated such APPJ gas configurations and our observations are consistent with enhanced $CH_4$ reactivity and greater rates of CO and $CO_2$ production. We will report our results in the future. At a catalyst temperature of 500 $^oC$, synergy effects can be observed (as shown in figure 12), since the surface $CH_n$ or vibrationally excited $CH_4$ [58] can be more easily decomposed to hydrocarbons with lower H content on the active catalyst sites, and the ROSs produced from the APPJ can enhance the thermal reaction as well. The plasma catalytic reactions at 500 $^oC$ include all the reactions discussed for a catalyst temperature of 25 $^oC$ with plasma, along with enhanced thermal catalytic reactions and possible enhancement effects due to plasma-surface interactions. These reactions contribute to the higher conversion rate, lower apparent activation energy and initiating temperature, and synergistic effect of plasma catalysis.

### 4.5.2. A possible picture of important surface reactions

Based on the discussion in section 4.5.1, we have attempted to bring the data together in first simplified models to explain possible reaction processes for different conditions examined here. This is shown in figure 15. It should be noted that while these processes are consistent with the

observations, they are also speculative since further characterization is required, e.g. on the state of the catalyst itself and the extent of plasma-induced gas phase reaction. Nevertheless, we offer this simplified schematic summary of possible processes since this may be helpful in terms of articulating further research questions that may shed light on the unknown mechanisms in plasma catalysis.

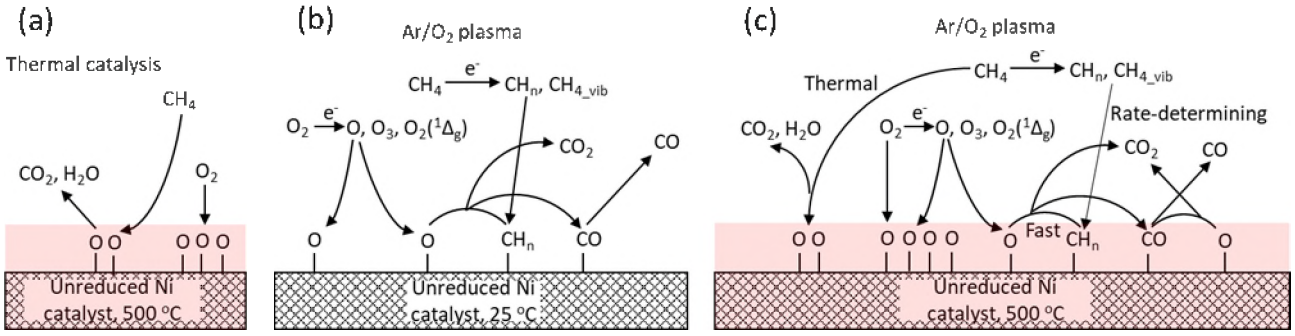


**Figure 15.** (a) Proposed thermal catalysis processes at a catalyst temperature of 500 °C for $CH_4/O_2$ system. $CH_4$ reacts with surface oxygen to produce $CO_2$ [22, 27, 64]. (b) Scheme of the plasma-assisted oxidation of $CH_4$ at a catalyst temperature of 25 °C, consistent with observations. $O_2$ (directly) and $CH_4$ (only by interaction with the plasma plume) are excited by plasma. Surface-adsorbed $CH_n$ species can be oxidized by atomic O to CO and $CO_2$. The latter may involve adsorbed oxygen. The catalyst is inactive in this case, and little formation of NiO takes place without the influence of plasma. (c) Scheme of the plasma catalysis reaction at a catalyst temperature of 500 °C. Spontaneous interaction of $O_2$ with the Ni catalyst produces NiO. Surface $CH_n$ is rapidly oxidized to CO and $CO_2$ by surface-adsorbed O on the activated catalyst. In addition, CO can also be further oxidized to $CO_2$ at an elevated catalyst temperature, as illustrated in figure 4b.

## 5. Conclusions

A non-thermal APPJ using different $Ar/O_2$ flows has been used to study plasma-catalyst interactions during oxidation of methane over a nickel catalyst at different temperatures. Analysis of FTIR-based gas phase and surface reactive-species measurements has shed light on the mechanisms of plasma-assisted catalytic $CH_4$ conversion. $CH_4$, CO and $CO_2$ were characterized downstream of the catalyst bed by FTIR, and the catalyst surface was analyzed by operando DRIFTS under the same conditions. By varying the $O_2$ flow rate through the APPJ source at catalyst temperatures of both 25 $^oC$ and 500 $^oC$, we found that the $O_2$ addition in the plasma can suppress the plasma-enabled $CH_4$ conversion (low catalyst temperature), while enhancing the thermal catalytic reaction (high catalyst temperature). The fact that plasma density increases both O atom generation and excitation of methane is consistent with the strong plasma power dependence observed. Reactive species in the plasma effluent analyzed by MBMS using an identical APPJ were correlated with the gas phase conversion and surface species measurements. By correlating the quantified ROSs fluxes (obtained by the characterization of the plasma effluent using MBMS) with the measured rates of $CH_4$ consumption and CO and $CO_2$ production, we found that the fluxes of the converted $CH_4$ and the CO and $CO_2$ products correlated best with the variation of the atomic O fluxes. This indicates that plasma-produced atomic oxygen is a key species responsible for the oxidation of $CH_4$ to CO and $CO_2$ for the experimental configuration used in the present work. The work presented here demonstrates a compelling correlation of the products from plasma-catalytic reactions with the incident reactive species flux from the plasma effluent for specific experimental conditions used here. Catalyst heating experiments showed that the apparent activation energy can be lowered by 40% with the assistance of the APPJ. DRIFTS spectra obtained on the catalyst revealed information on surface

species. A blue shift of the CO vibrational frequency from the gas phase CO to surface CO was observed. A possible explanation of this is the change of the oxidation state of the nickel catalyst. We also found the abundance of surface CO followed that of surface $CH_n$ species at a catalyst temperature of 25 °C. This indicates that $CH_n$ is adsorbed and then transformed into CO. It also suggests that the excitation of $CH_4$ to form $CH_n$ on the catalyst surface mirrors the flux of O atoms to the catalyst surface, but that oxidation to CO is limited by the arrival rate of O atoms. The lack of appreciable surface $CH_n$ along with increased surface CO at a catalyst temperature of 500 °C can be explained by additional thermal oxidation and indicates that the decomposition of $CH_4$ to $CH_n$ may be the rate-determining step at elevated catalyst temperature. Based on the observation, a conceptual model for thermal catalysis, plasma-induced reaction at 25 °C and plasma catalysis at 500 °C has been built to understand the plasma-catalyst interaction.

**6. Supplemental material**

Due to the very large dissociation energy of $CH_4$, only a few reactive species produced by the plasma will dissociate $CH_4$ in the gas-phase at sufficiently high rates to be impactful, including energetic electrons and O atoms. In this study the $CH_4$ is not fed through the ionized plasma jet, the entrainment of $CH_4$ into the plasma jet effluent is necessary for gas phase dissociation. To assess the importance of gas phase $CH_4$ dissociation in the afterglow region of APPJ, a simple estimation was performed to evaluate the possible roles of electrons and O atoms based on rate coefficients of the following $CH_4$ dissociation reactions:

$$e^- + CH_4 \rightarrow e^- + CH_3 + H,\ k_1 = f(T_e) \qquad \text{(R1)}$$

$$O + CH_4 \rightarrow CH_3 + OH,\ k_2 = 2.26\times10^{-12}\,(T/298)^{2.20}\exp(-3819.84/T)\ \text{cm}^3\ \text{s}^{-1} \qquad \text{(R2)}$$

The role of other dominant reactive species such as $O_2(a^1\Delta_g)$ and $O_3$ can be ruled out due to their low energies, although recombination of $O_3$ can lead to the formation of O in the plasma effluent. The threshold energy of R1 is ~10 eV according to the cross-section data from [68]. Assuming the electron temperature of 2 eV, consistent with the measurements in [37] using a similar plasma jet in the Ar+0.5% $O_2$ + 0.33% $CH_4$ gas composition, the non-Maxwellian properties of electron energy distribution function (EEDF) deplete the high energy electrons (>10 eV), and an upper limit of $k_1$ is calculated to be $5\times10^{-14}$ $cm^3$ $s^{-1}$ with BOLSIG+ (12/2019) [69] using the PHELPS database from LXCat [70]. On the other hand, the rate coefficient of the competing reaction $k_2$ at 350 K (gas temperature in the jet effluents) is calculated to be $5.9\times10^{-17}$ $cm^3/s$. Note that $CH_4$ mostly diffuses into the jet effluent instead of the active plasma region, particularly for larger $O_2$ concentrations with shorter plasma plume length. At the tip of the plasma plume, the O density will be in excess of $2\times10^{16}$ $cm^{-3}$ and the electron density will be ~ $10^{12}$ $cm^3/s$. This suggests the dissociation of $CH_4$ by O density is most likely more effective than electron-induced $CH_4$ dissociation. This might suggest significantly different conditions compared to a DBD system where transient higher electron temperatures are obtained and $CH_4$ dissociation has been attributed to electron-induced reactions [58]. Nevertheless, the characteristic timescale of these reactions remains slow for the investigated plasma conditions to fully explain the gas phase conversion and other processes involving excited state molecules, such as $O(^1D)$, cannot be excluded. A further analysis requires detailed modeling which is out of scope of this work.

## 7. Acknowledgments

We gratefully acknowledge the financial support by National Science Foundation (CBET-1703211 and CBET-1703439) and US Department of Energy (DE-SC0020232). We thank

Pingshan Luan, Andrew J. Knoll, Kang-Yi Lin and Sang-Jin Chung for their helpful discussions and support.

# Reference


1. Whitehead, J.C., *Plasma–catalysis: the known knowns, the known unknowns and the unknown unknowns.* Journal of Physics D: Applied Physics, 2016. **49**(24): p. 243001.
2. Goujard, V., J. Tatibouet, and C. Batiot-Dupeyrat, *Influence of the Plasma Power Supply Nature on the Plasma–Catalyst Synergism for the Carbon Dioxide Reforming of Methane.* IEEE Transactions on Plasma Science, 2009. **37**(12): p. 2342-2346.
3. Nozaki, T., et al., *Kinetic analysis of the catalyst and nonthermal plasma hybrid reaction for methane steam reforming.* Energy & Fuels, 2007. **21**(5): p. 2525-2530.
4. Whitehead, J.C., *Plasma catalysis: A solution for environmental problems.* Pure and Applied Chemistry, 2010. **82**(6): p. 1329-1336.
5. Kim, H.-H., A. Ogata, and S. Futamura, *Oxygen partial pressure-dependent behavior of various catalysts for the total oxidation of VOCs using cycled system of adsorption and oxygen plasma.* Applied Catalysis B: Environmental, 2008. **79**(4): p. 356-367.
6. Xu, X.X., et al., *High-efficiency non-thermal plasma-catalysis of cobalt incorporated mesoporous MCM-41 for toluene removal.* Catalysis Today, 2017. **281**: p. 527-533.
7. Ranji-Burachaloo, H., et al., *Synergetic effects of plasma and metal oxide catalysts on diesel soot oxidation.* Applied Catalysis B-Environmental, 2016. **182**: p. 74-84.
8. Brune, L., et al., *Dry reforming of methane via plasma-catalysis: influence of the catalyst nature supported on alumina in a packed-bed DBD configuration.* Journal of Physics D-Applied Physics, 2018. **51**(23).
9. Song, L.J., Y.L. Kong, and X.H. Li, *Hydrogen production from partial oxidation of methane over dielectric barrier discharge plasma and NiO/gamma-Al2O3 catalyst.* International Journal of Hydrogen Energy, 2017. **42**(31): p. 19869-19876.
10. Dahiru, U.H., et al., *Removal of cyclohexane as a toxic pollutant from air using a non-thermal plasma: Influence of different parameters.* Journal of Environmental Chemical Engineering, 2021. **9**(1): p. 105023.
11. Zhang, S., et al., *Mechanistic aspects of plasma-enhanced catalytic methane decomposition by time-resolved operando diffuse reflectance infrared Fourier transform spectroscopy.* Journal of Physics D-Applied Physics, 2020. **53**(21).
12. Iwamoto, M., et al., *Ammonia Synthesis on Wool-Like Au, Pt, Pd, Ag, or Cu Electrode Catalysts in Nonthermal Atmospheric-Pressure Plasma of N-2 and H-2.* Acs Catalysis, 2017. **7**(10): p. 6924-6929.
13. Aihara, K., et al., *Remarkable catalysis of a wool-like copper electrode for NH3 synthesis from N-2 and H-2 in non-thermal atmospheric plasma.* Chemical Communications, 2016. **52**(93): p. 13560-13563.
14. Wei, Z. and C.-j. Liu, *Synthesis of monodisperse gold nanoparticles in ionic liquid by applying room temperature plasma.* Materials Letters, 2011. **65**(2): p. 353-355.
15. Neyts, E.C., et al., *Plasma Catalysis: Synergistic Effects at the Nanoscale.* Chemical Reviews, 2015. **115**(24): p. 13408-13446.
16. Knoll, A.J., et al., *Infrared studies of gas phase and surface processes of the enhancement of catalytic methane decomposition by low temperature plasma.* Journal of Physics D-Applied Physics, 2019. **52**(22).
17. Hofmann, S., et al., *Power dissipation, gas temperatures and electron densities of cold atmospheric pressure helium and argon RF plasma jets.* Plasma Sources Science & Technology, 2011. **20**(6): p. 065010.

18. Holzer, F., U. Roland, and F.D. Kopinke, *Combination of non-thermal plasma and heterogeneous catalysis for oxidation of volatile organic compounds: Part 1. Accessibility of the intra-particle volume.* Applied Catalysis B: Environmental, 2002. **38**(3): p. 163-181.
19. Luan, P. and G.S. Oehrlein, *Interaction of long-lived reactive species from cold atmospheric pressure plasma with polymers: Chemical modification by ozone and reactive oxygen-nitrogen species.* Journal of Vacuum Science & Technology A, 2019. **37**(5): p. 051303.
20. Jiang, J.K. and P.J. Bruggeman, *Absolute ion density measurements in the afterglow of a radiofrequency atmospheric pressure plasma jet.* Journal of Physics D-Applied Physics, 2021. **54**(15).
21. Ma, R.S., B. Xu, and X. Zhang, *Catalytic partial oxidation (CPOX) of natural gas and renewable hydrocarbons/oxygenated hydrocarbons-A review.* Catalysis Today, 2019. **338**: p. 18-30.
22. Dissanayake, D., et al., *PARTIAL OXIDATION OF METHANE TO CARBON-MONOXIDE AND HYDROGEN OVER A NI/AL2O3 CATALYST.* Journal of Catalysis, 1991. **132**(1): p. 117-127.
23. Mhadeshwar, A.B. and D.G. Vlachos, *A Catalytic Reaction Mechanism for Methane Partial Oxidation at Short Contact Times, Reforming, and Combustion, and for Oxygenate Decomposition and Oxidation on Platinum.* Industrial & Engineering Chemistry Research, 2007. **46**(16): p. 5310-5324.
24. Prettre, M., C. Eichner, and M. Perrin, *The catalytic oxidation of methane to carbon monoxide and hydrogen.* Transactions of the Faraday Society, 1946. **42**(0): p. 335b-339.
25. Elmasides, C. and X.E. Verykios, *Mechanistic Study of Partial Oxidation of Methane to Synthesis Gas over Modified Ru/TiO2 Catalyst.* Journal of Catalysis, 2001. **203**(2): p. 477-486.
26. Lu, Y., et al., *Mechanistic investigations on the partial oxidation of methane to synthesis gas over a nickel-on-alumina catalyst.* Applied Catalysis A: General, 1998. **174**(1): p. 121-128.
27. Hu, Y.H. and E. Ruckenstein, *Isotopic GCMS Study of the Mechanism of Methane Partial Oxidation To Synthesis Gas.* The Journal of Physical Chemistry A, 1998. **102**(51): p. 10568-10571.
28. Chu, Y., et al., *Partial oxidation of methane to carbon monoxide and hydrogen over NiO/La2O3/γ-Al2O3 catalyst.* Applied Catalysis A: General, 1996. **134**(1): p. 67-80.
29. Zhang, S. and G.S. Oehrlein, *From thermal catalysis to plasma catalysis: a review of surface processes and their characterizations.* Journal of Physics D: Applied Physics, 2021. **54**(21): p. 213001.
30. Rodrigues, A., J.-M. Tatibouët, and E. Fourré, *Operando DRIFT Spectroscopy Characterization of Intermediate Species on Catalysts Surface in VOC Removal from Air by Non-thermal Plasma Assisted Catalysis.* Plasma Chemistry and Plasma Processing, 2016. **36**(4): p. 901-915.
31. Jiang, J.K., et al., *Absolute spatially and time-resolved O, O-3, and air densities in the effluent of a modulated RF-driven atmospheric pressure plasma jet obtained by molecular beam mass spectrometry.* Plasma Processes and Polymers, 2020. **17**(6).
32. Zhang, S.Q., et al., *Spatially resolved ozone densities and gas temperatures in a time modulated RF driven atmospheric pressure plasma jet: an analysis of the production and destruction mechanisms.* Journal of Physics D-Applied Physics, 2013. **46**(20): p. 205202.
33. Gaens, W.V., P.J. Bruggeman, and A. Bogaerts, *Numerical analysis of the NO and O generation mechanism in a needle-type plasma jet.* New Journal of Physics, 2014. **16**(6): p. 063054.
34. Zhang, S., et al., *Temporally resolved ozone distribution of a time modulated RF atmospheric pressure argon plasma jet: flow, chemical reaction, and transient vortex.* Plasma Sources Science and Technology, 2015. **24**(4): p. 045015.
35. Jiang, J.K., Y.A. Gonzalvo, and P.J. Bruggeman, *Spatially resolved density measurements of singlet delta oxygen in a non-equilibrium atmospheric pressure plasma jet by molecular beam mass spectrometry.* Plasma Sources Science & Technology, 2020. **29**(4).

36. Rothman, L.S., et al., *The HITRAN2012 molecular spectroscopic database.* Journal of Quantitative Spectroscopy & Radiative Transfer, 2013. **130**: p. 4-50.
37. Gessel, B.v., R. Brandenburg, and P. Bruggeman, *Electron properties and air mixing in radio frequency driven argon plasma jets at atmospheric pressure.* Applied Physics Letters, 2013. **103**(6): p. 064103.
38. Jiang, J. and P.J. Bruggeman, *Spatially resolved absolute densities of reactive species and positive ion flux in He-O2 RF-driven atmospheric pressure plasma jet: touching and non-touching with dielectric substrate.* Journal of Physics D: Applied Physics, 2020. **53**(28): p. 28LT01.
39. Sirita, J., S. Phanichphant, and F.C. Meunier, *Quantitative analysis of adsorbate concentrations by diffuse reflectance FT-IR.* Analytical Chemistry, 2007. **79**(10): p. 3912-3918.
40. Binet, C., M. Daturi, and J.-C. Lavalley, *IR study of polycrystalline ceria properties in oxidised and reduced states.* Catalysis Today, 1999. **50**(2): p. 207-225.
41. Stere, C., et al., *A design of a fixed bed plasma DRIFTS cell for studying the NTP-assisted heterogeneously catalysed reactions.* Catalysis Science & Technology, 2020. **10**(5): p. 1458-1466.
42. Demoulin, O., M. Navez, and P. Ruiz, *Investigation of the behaviour of a Pd/γ-Al2O3 catalyst during methane combustion reaction using in situ DRIFT spectroscopy.* Applied Catalysis A: General, 2005. **295**(1): p. 59-70.
43. Li, Z., G. Xu, and G.B. Hoflund, *In situ IR studies on the mechanism of methane oxidation over Pd/Al2O3 and Pd/Co3O4 catalysts.* Fuel Processing Technology, 2003. **84**(1): p. 1-11.
44. Guo, J., et al., *DRIFTS Study on Adsorption and Activation of CH4 and CO2 over Ni/SiO2 Catalyst with Various Ni Particle Sizes.* Chinese Journal of Catalysis, 2007. **28**(1): p. 22-26.
45. Jia, Z.X., et al., *Dynamic probing of plasma-catalytic surface processes: Oxidation of toluene on CeO2.* Plasma Processes and Polymers, 2017. **14**(6).
46. Stere, C.E., et al., *Probing a Non-Thermal Plasma Activated Heterogeneously Catalyzed Reaction Using in Situ DRIFTS-MS.* ACS Catalysis, 2015. **5**(2): p. 956-964.
47. Vayssilov, G.N., et al., *Reassignment of the Vibrational Spectra of Carbonates, Formates, and Related Surface Species on Ceria: A Combined Density Functional and Infrared Spectroscopy Investigation.* The Journal of Physical Chemistry C, 2011. **115**(47): p. 23435-23454.
48. Tsyganenko, A.A., T.A. Rodionova, and V.N. Filimonov, *INFRARED STUDIES OF LOW-TEMPERATURE ADSORPTION OF OXYGEN ON NIO SURFACE.* Reaction Kinetics and Catalysis Letters, 1979. **11**(2): p. 113-116.
49. Meunier, F.C., et al., *Quantitative analysis of the reactivity of formate species seen by DRIFTS over a Au/Ce(La)O-2 water-gas shift catalyst: First unambiguous evidence of the minority role of formates as reaction intermediates.* Journal of Catalysis, 2007. **247**(2): p. 277-287.
50. Jiang, J. and P.J. Bruggeman, *Tuning plasma parameters to control reactive species fluxes to substrates in the context of plasma catalysis.* Journal of Physics D: Applied Physics, 2021. **54**(21): p. 214005.
51. Fei, X.M., et al., *Influence of Additive Gas on Electrical and Optical Characteristics of Non-equilibrium Atmospheric Pressure Argon Plasma Jet.* Plasma Science & Technology, 2011. **13**(5): p. 575-582.
52. Zhang, S.S., et al., *Atmospheric pressure RF plasma jet : characterization of flow and O2 chemistry.* 2015, Technische Universiteit Eindhoven: Eindhoven.
53. Mei, D.H., S.Y. Liu, and X. Tu, *CO2 reforming with methane for syngas production using a dielectric barrier discharge plasma coupled with Ni/gamma-Al2O3 catalysts: Process optimization through response surface methodology.* Journal of Co2 Utilization, 2017. **21**: p. 314-326.

54. Knoll, A.J., et al., *Cold Atmospheric Pressure Plasma VUV Interactions With Surfaces: Effect of Local Gas Environment and Source Design.* Plasma Processes and Polymers, 2016. **13**(11): p. 1069-1079.
55. Luan, P., et al., *Model polymer etching and surface modification by a time modulated RF plasma jet: role of atomic oxygen and water vapor.* Journal of Physics D: Applied Physics, 2017. **50**(3): p. 03LT02.
56. Kondeti, V.S.S.K., et al., *O·, H·, and ·OH radical etching probability of polystyrene obtained for a radio frequency driven atmospheric pressure plasma jet.* Journal of Vacuum Science & Technology A, 2020. **38**(3): p. 033012.
57. Geng, H.J., et al., *Effects of O-2/CH4 ratio on methane catalytic combustion over Cu/gamma-Al2O3 particles.* International Journal of Hydrogen Energy, 2016. **41**(40): p. 18282-18290.
58. Nozaki, T., et al., *Dissociation of vibrationally excited methane on Ni catalyst: Part 1. Application to methane steam reforming.* Catalysis Today, 2004. **89**(1): p. 57-65.
59. Politzer, P. and S.D. Kasten, *An investigation of the high-frequency form of carbon monoxide chemisorbed on nickel oxide.* Surface Science, 1973. **36**(1): p. 186-194.
60. Hoffmann, F.M., *Infrared reflection-absorption spectroscopy of adsorbed molecules.* Surface Science Reports, 1983. **3**(2): p. 107-192.
61. Chakarova, K., et al., *Co-ordination chemistry of palladium cations in Pd-H-ZSM-5 as revealed by FTIR spectra of adsorbed and co-adsorbed probe molecules (CO and NO).* Physical Chemistry Chemical Physics, 2004. **006**(13): p. 3702-3709.
62. Martínez-Arias, A., et al., *New Pd/CexZr1−xO2/Al2O3 three-way catalysts prepared by microemulsion: Part 2. In situ analysis of CO oxidation and NO reduction under stoichiometric CO+NO+O2.* Applied Catalysis B: Environmental, 2001. **31**(1): p. 51-60.
63. Lu, Y., et al., *Origin of the High CO Oxidation Activity on CeO2 Supported Pt Nanoparticles: Weaker Binding of CO or Facile Oxygen Transfer from the Support?* ChemCatChem, 2020. **12**(6): p. 1726-1733.
64. Hu, Y.H. and E. Ruckenstein, *Multiple Transient Response Methods To Identify Mechanisms of Heterogeneous Catalytic Reactions.* Accounts of Chemical Research, 2003. **36**(10): p. 791-797.
65. Hu, Y.H. and E. Ruckenstein, *Broadened Pulse-Step Change−Isotopic Sharp Pulse Analysis of the Mechanism of Methane Partial Oxidation to Synthesis Gas.* The Journal of Physical Chemistry B, 1998. **102**(1): p. 230-233.
66. Hu, C., et al., *Temperature-programmed FT-IR study of the adsorption of CO and co-adsorption of CO and H2 on NiAl2O3.* Journal of Molecular Catalysis A: Chemical, 1996. **110**(2): p. 163-169.
67. Mukerji, R.J., A.S. Bolina, and W.A. Brown, *A RAIRS and TPD investigation of the adsorption of CO on Pt{211}.* Surface Science, 2003. **527**(1): p. 198-208.
68. Winters, H.F., *Dissociation of methane by electron impact.* The Journal of Chemical Physics, 1975. **63**(8): p. 3462-3466.
69. Hagelaar, G.J.M. and L.C. Pitchford, *Solving the Boltzmann equation to obtain electron transport coefficients and rate coefficients for fluid models.* Plasma Sources Science and Technology, 2005. **14**(4): p. 722-733.
70. Pitchford, L.C., et al., *LXCat: an Open-Access, Web-Based Platform for Data Needed for Modeling Low Temperature Plasmas.* Plasma Processes and Polymers, 2017. **14**(1-2): p. 1600098.